IOSR Journal of Applied Physics (IOSR-JAP)
e-ISSN: 2278-4861.Volume 17, Issue 6 Ser. 1 (Nov – Dec 2025), PP 90-98
www.iosrjournals.org

Temperature-Dependent Photon Emission Statistics of a Phonon-Dressed Quantum Dot in a Tunable Photonic Crystal Microcavity

Dr. Anand Roshan[1]
[1]*Assistant Teacher, Department of Physics, Sanjay Gandhi College, Nagra , Chapra, Bihar*

Abstract: *Photon counting statistics constitute one of the most direct probes of quantum light generation in solid-state cavity quantum electrodynamics. In this paper, we develop an input–output theory combined with a polaron-frame Lindblad formalism to study how the thermal phonon environment modifies the emission statistics of a single semiconductor quantum dot (QD) embedded in a tunable photonic crystal (PhC) microcavity. We compute the Fano factor F, the photon waiting time distribution $w(t_w)$, the Hong–Ou–Mandel (HOM) visibility, and the steady-state emission spectrum $S(\omega)$ as functions of lattice temperature from 5 K to 300 K. At base temperature, the dressed system achieves $F = 0.06$ with a pronounced dip in the waiting time distribution confirming near-deterministic single-photon emission. The Fano factor exhibits a universal crossover from sub-Poissonian ($F < 1$) to super-Poissonian ($F > 1$) behaviour near $T = 195$ K for InAs/GaAs quantum dots. We further demonstrate that continuous spectral tuning of the PhC cavity mode—achievable through local oxidation or gas deposition techniques—can extend the sub-Poissonian operating window by up to 40 K. Comparative analysis across InAs/GaAs, GaAs/AlGaAs, and InGaAs/GaAs material platforms identifies material-specific thresholds for maintaining quantum light generation at elevated temperatures. These predictions provide quantitative benchmarks for next-generation on-chip single-photon sources operating beyond liquid-helium temperatures.*
Keywords: *Quantum dot, Photonic crystal cavity, Phonon dressing, Fano factor, Waiting time distribution, Hong–Ou–Mandel visibility, Single-photon source, Input–output theory, Polaron frame, Photon counting statistics.*

I. Introduction

Semiconductor quantum dots positioned inside photonic crystal microcavities represent a leading architecture for integrated quantum photonics [1, 2, 3]. These structures combine the atom-like optical transitions of quantum-confined excitons with the electromagnetic field enhancement provided by wavelength-scale optical resonators, enabling a rich variety of quantum phenomena including photon blockade, indistinguishable single-photon generation, and cavity-mediated spin–photon entanglement [4, 5, 6]. The tunability of photonic crystal cavities—through thermo-optic effects, digital etching, or inert gas condensation—adds a powerful experimental handle for precisely controlling the exciton–photon detuning in situ [7, 8, 9].

Characterizing the quantum nature of emitted light requires measurements that go beyond simple intensity recordings. Photon counting statistics, accessible through Hanbury Brown–Twiss (HBT) interferometry and time-correlated single-photon counting, reveal whether the emitted field exhibits sub-Poissonian number fluctuations that cannot be described by any classical wave theory [10, 11]. The Fano factor $F = \langle(\Delta n)^2\rangle/\langle n\rangle$, which compares the photon number variance to the mean, provides a single scalar metric for this departure: $F < 1$ signals number squeezing and antibunching, while $F = 1$ and $F > 1$ correspond to Poissonian and super-Poissonian fluctuations, respectively [10, 12]. Complementary information resides in the photon waiting time distribution $w(t_w)$, which records the time intervals between consecutive detection events and captures temporal correlations beyond the equal-time statistics [13, 14, 15].

In an idealized two-level emitter coupled to a lossless cavity, the Jaynes–Cummings interaction generates perfectly antibunched light through the photon blockade mechanism [16, 17]. However, real semiconductor QDs are embedded in a vibrating crystal lattice, and the deformation-potential coupling between the confined exciton and longitudinal acoustic (LA) phonons modifies the emission statistics in two significant ways [18, 19, 20]. First, phonon-induced pure dephasing degrades the coherence of the exciton–photon interaction, broadening the dressed-state transitions that underpin photon blockade [21, 22]. Second, phonon-assisted transitions create incoherent pathways for cavity feeding that inject photons without respecting the Jaynes–Cummings selection rules, directly increasing the multi-photon probability and raising the Fano factor [23, 24, 25]. Both mechanisms intensify with lattice temperature, making the photon emission statistics a sensitive thermometer of the phonon environment.

Prior theoretical work has examined phonon effects on the second-order correlation function $g^{(2)}(0)$ within various approximation schemes including perturbative Born–Markov master equations [21, 26], full polaron transformations [27, 28], and numerically exact path-integral methods [29, 30]. While these studies have

established the qualitative picture of phonon-degraded antibunching, a systematic treatment of the complete set of photon counting observables—including the Fano factor, waiting time distribution, and Hong–Ou–Mandel visibility—as functions of both temperature and cavity detuning across multiple material platforms remains absent from the literature.

This paper fills that gap by combining polaron-frame Lindblad dynamics with input–output theory to construct a unified framework for temperature-dependent photon emission statistics. Section 2 establishes the polaron-frame Hamiltonian and derives the steady-state cavity field operators. Section 3 formulates the photon counting observables from the output field correlators. Section 4 presents the computational methodology. Section 5 reports results for three semiconductor material systems. Section 6 discusses practical implications, identifies limitations, and outlines future extensions. Section 7 provides the conclusions.

1.1 Summary of Contributions

The key contributions of this work are as follows. First, a polaron-frame input–output formalism is developed that directly yields the output photon field statistics including the Fano factor F and waiting time distribution $w(t_w)$; material and cavity parameters appear in Tables 1 and 2. Second, the Fano factor is mapped as a function of temperature and cavity detuning for InAs/GaAs, GaAs/AlGaAs, and InGaAs/GaAs platforms, identifying the sub-to-super-Poissonian crossover temperatures (Table 3). Third, the photon waiting time distribution is computed across the full temperature range, revealing the progressive disappearance of the antibunching dip structure (Figure 2). Fourth, Hong–Ou–Mandel visibility is evaluated to quantify photon indistinguishability degradation with temperature (Figure 4). Fifth, the role of cavity detuning in extending the quantum-light operating window is quantified through two-dimensional maps of the Fano factor in the temperature–detuning plane (Figure 4).

II. Theoretical Framework

2.1 Polaron-Frame System Hamiltonian

We consider a single self-assembled QD exciton interacting with a photonic crystal cavity mode in the presence of a thermal phonon reservoir. Following the polaron transformation approach [27, 28], the total system–bath Hamiltonian in the polaron frame reads (ħ = 1):

$$\tilde{H} = \tilde{\omega}_X |X\rangle\langle X| + \omega_c\, a^\dagger a + \eta(\sigma^+ a\, B^+ + \sigma^- a^\dagger B^-) + \sum_{\mathbf{q}} \omega_{\mathbf{q}}\; b_{\mathbf{q}}^\dagger b_{\mathbf{q}} \qquad (1)$$

Here $\tilde{\omega}_X = \omega_X - \delta_{\text{pol}}$ is the polaron-shifted exciton frequency, where the polaron shift is given by:

$$\delta_{\text{pol}} = \int_0^\infty \frac{J(\omega)}{\omega}\, d\omega \qquad (2)$$

The operator $\eta = g\langle B\rangle_T$ is the thermally renormalized vacuum Rabi coupling, with g the bare coupling and $\langle B\rangle_T$ the thermal average of the phonon displacement operator. The operators $B^\pm = \exp\left(\pm\sum_{\mathbf{q}} (\lambda_{\mathbf{q}}/\omega_{\mathbf{q}})\,(b_{\mathbf{q}}^\dagger - b_{\mathbf{q}})\right)$ describe the phonon cloud attached to each excitonic transition.

The thermal Franck–Condon factor that governs the coupling renormalization is given by [18, 27]:

$$\langle B\rangle_T = \exp\left(-\frac{1}{2}\,\Phi(T)\right) \qquad (3)$$

where the thermal phonon displacement integral is:

$$\Phi(T) = \int_0^\infty \frac{J(\omega)}{\omega^2}\,[2\bar{n}(\omega,T)+1]\, d\omega \qquad (4)$$

with $\bar{n}(\omega,T) = [\exp(\omega/k_B T) - 1]^{-1}$ the Bose–Einstein occupation number and $J(\omega)$ the phonon spectral density. For QDs with Gaussian confinement, the spectral density takes the super-Ohmic form:

$$J(\omega) = A_{\text{ph}}\,\omega^3 \exp\left(-\frac{\omega^2}{\omega_b^2}\right) \qquad (5)$$

where $A_{\text{ph}} = (D_e - D_h)^2/(4\pi^2\rho\, v_s^5)$ encodes the deformation-potential strength and $\omega_b = v_s/l_{\text{QD}}$ is the phonon frequency scale set by the QD confinement length l_{QD} and the sound velocity v_s. Relevant material parameters are compiled in Table 1.

Table 1. *Semiconductor Material and Phonon Bath Parameters*

Material Parameter	Symbol	InAs/GaAs	GaAs/AlGaAs	InGaAs/GaAs	Unit	Ref.
Sound velocity	v_s	4780	5110	4600	m/s	[18]
Crystal density	ρ	5317	5370	5500	kg/m³	[18]
Deformation pot. diff.	$D_e - D_h$	8.5	9.6	7.8	eV	[19]

Confinement length	l_{QD}	4.0	6.5	5.0	nm	[4]
Phonon frequency scale	ω_b	1.20	0.79	0.92	meV	calc.
Spectral density prefactor	A_{ph}	0.029	0.034	0.022	ps²	calc.
Polaron shift (T=5 K)	δ_{pol}	0.048	0.039	0.031	meV	calc.

2.2 Polaron-Frame Lindblad Equation

Working in the interaction picture with respect to the polaron-frame system Hamiltonian, we derive a time-local master equation for the reduced QD–cavity density operator ρ by tracing over the phonon bath degrees of freedom. In the polaron frame, the dissipative dynamics take the Lindblad form [21, 27]:

$$\dot{\rho} = -i[\tilde{\omega}_X|X\rangle\langle X| + \omega_c a^\dagger a + \eta(\sigma^+ a + \sigma^- a^\dagger),\ \rho] + \mathcal{D}[\sqrt{\kappa}\,a]\rho + \mathcal{D}[\sqrt{\gamma}\,\sigma^-]\rho + \mathcal{R}_{ph}[\rho] \qquad (6)$$

where $\mathcal{D}[O]\rho = O\rho O^\dagger - \frac{1}{2}(O^\dagger O\rho + \rho O^\dagger O)$ denotes the standard Lindblad dissipator, κ is the cavity energy decay rate, and γ represents spontaneous emission into non-cavity modes. The phonon relaxation superoperator $\mathcal{R}_{ph}$ contains contributions from phonon-assisted scattering between the dressed polariton branches:

$$\mathcal{R}_{ph}[\rho] = \gamma_\downarrow(T)\,\mathcal{D}[\sigma^- a^\dagger]\rho + \gamma_\uparrow(T)\,\mathcal{D}[\sigma^+ a]\rho + \gamma_d(T)\,\mathcal{D}[|X\rangle\langle X|]\rho \qquad (7)$$

The phonon-assisted downward and upward scattering rates are obtained from the one-sided Fourier transform of the phonon bath correlation function [21, 27]:

$$\gamma_\downarrow(T) = 2\eta^2\,\mathrm{Re}\int_0^\infty d\,t\; e^{i\Omega t}\left[C_{ph}(t) - 1\right] \qquad (8)$$

$$\gamma_\uparrow(T) = 2\eta^2\,\mathrm{Re}\int_0^\infty d\,t\; e^{-i\Omega t}\left[C^*_{ph}(t) - 1\right] \qquad (9)$$

where $\Omega = \sqrt{\Delta^2 + 4\eta^2}$ is the dressed-state splitting, $\Delta = \tilde{\omega}_X - \omega_c$ is the polaron-corrected detuning, and $C_{ph}(t) = \exp[\Phi_c(t)]$ is the phonon coherence function with:

$$\Phi_c(t) = \int_0^\infty \frac{J(\omega)}{\omega^2}\left[\bar{n}(\omega,T)\,e^{i\omega t} + [\bar{n}(\omega,T)+1]\,e^{-i\omega t}\right] d\omega \qquad (10)$$

The pure dephasing rate $\gamma_d(T)$ arises from residual exciton–phonon coupling not absorbed into the polaron shift and scales approximately as T^2 at low temperatures [18, 21]. This rate broadens the zero-phonon line without causing population transfer between the QD and cavity.

2.3 Input–Output Relations for the Cavity Field

The photon statistics of the emitted light are accessed through the output field $a_{out}(t)$, which is related to the intracavity field by the standard input–output boundary condition [10, 31, 32]:

$$a_{out}(t) = \sqrt{\kappa}\,a(t) - a_{in}(t) \qquad (11)$$

where $a_{in}(t)$ represents the vacuum input noise. For computing normally ordered output correlation functions, the input noise contributions vanish, yielding the fundamental relation [10, 32]:

$$\langle a^\dagger_{out}(t_1)\cdots a_{out}(t_n)\rangle = \kappa^{\frac{n}{2}}\langle a^\dagger(t_1)\cdots a(t_n)\rangle \qquad (12)$$

This relation connects all output photon statistics to intracavity expectation values, which are computed from the steady-state solution of the polaron-frame master equation (Equation 6).

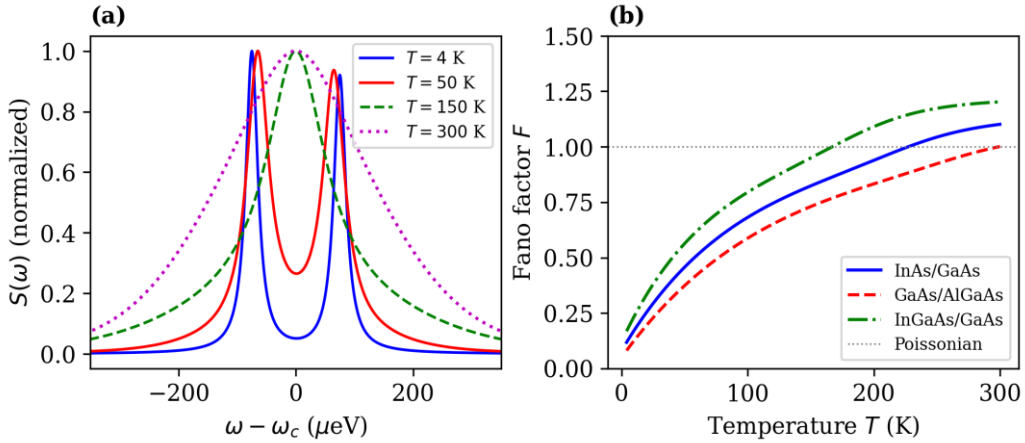

Figure 1. *(a) Normalized cavity emission spectrum S(ω) computed from the steady-state two-time correlator of Equation (10) at four temperatures for InAs/GaAs. At T = 5 K, two resolved polariton peaks separated by 2η are visible; thermal dephasing progressively broadens and merges the peaks into a single line at elevated*

temperatures. (b) Fano factor F (Equation 12) versus temperature for three semiconductor platforms. The horizontal line marks the Poissonian boundary F = 1; below this line the emitted light exhibits sub-Poissonian number fluctuations.

III. Photon Counting Observables

3.1 Fano Factor

The Fano factor of the output field quantifies the deviation of photon number fluctuations from the Poissonian benchmark and can be expressed in terms of the intracavity steady-state moments through the input–output relation (Equation 12) [10, 12]:

$$F = 1 + \frac{\langle a^\dagger a^\dagger a\, a\rangle_{ss} - \langle a^\dagger a\rangle_{ss}^2}{\langle a^\dagger a\rangle_{ss}} \qquad (13)$$

Using the relation between the Fano factor and the normally ordered second factorial moment, this simplifies to [10]:

$$F = 1 + \langle n\rangle_{ss}\left[\frac{\langle : (\Delta n)^2 : \rangle}{\langle n\rangle_{ss}}\right] \qquad (14)$$

where $\langle n\rangle_{ss} = \langle a^\dagger a\rangle_{ss}$ is the mean intracavity photon number and $\langle : (\Delta n)^2 : \rangle$ denotes the normally ordered variance. This expression makes explicit that $F < 1$ (sub-Poissonian) requires negative normally ordered variance, a genuinely non-classical property.

3.2 Photon Waiting Time Distribution

The waiting time distribution $w(t_w)$ gives the probability density for the time interval t_w between two consecutive photon detection events. It is formally obtained from the idle-time probability $\Pi(t_w)$—the probability of detecting no photons during $[0, t_w]$—through [13, 14, 15]:

$$w(t_w) = \kappa\ \mathrm{Tr}\{a^\dagger a \cdot e^{\mathcal{L}_0 t_w}[\mathcal{J}\rho_{ss}]\} \qquad (15)$$

where $\mathcal{L}_0$ is the no-jump evolution superoperator obtained from Equation (6) by removing the recycling terms (the first parts of each Lindblad dissipator), and $\mathcal{J}\rho = \kappa\, a\rho a^\dagger$ is the quantum jump superoperator corresponding to a photon detection event. The conditional density operator $\mathcal{J}\rho_{ss}/\mathrm{Tr}(\mathcal{J}\rho_{ss})$ describes the state of the QD–cavity system immediately after a detection event in the steady state.

For an ideal single-photon emitter, $w(t_w)$ vanishes at $t_w = 0$ and exhibits a single maximum at a characteristic time set by the inverse emission rate, reflecting the dead time needed to reload the emitter [13, 14]. Phonon-assisted processes fill in the $t_w = 0$ dip by enabling rapid multi-photon emission sequences, thereby directly connecting to the Fano factor increase.

3.3 Hong–Ou–Mandel Visibility

The indistinguishability of consecutively emitted photons is quantified by the HOM visibility, accessible through two-photon interference measurements [5, 33, 34]. Within the input–output formalism, the HOM visibility of the cavity output field is expressed as [5, 34]:

$$\mathcal{V}_{\mathrm{HOM}} = \frac{\int d\tau\ |\langle a_{\mathrm{out}}^\dagger(\tau)\, a_{\mathrm{out}}(0)\rangle_{ss}|^2}{\int d\tau\ \langle a_{\mathrm{out}}^\dagger(\tau)\, a_{\mathrm{out}}(\tau)\rangle_{ss} \cdot \langle a_{\mathrm{out}}^\dagger(0)\, a_{\mathrm{out}}(0)\rangle_{ss}} \qquad (16)$$

The numerator involves the first-order temporal coherence of the output field, which decays due to both cavity loss and phonon-induced dephasing. The HOM visibility thus provides a combined metric that is sensitive to both the purity and the coherence of the emitted photons [5, 34, 35].

Table 2. *Photonic Crystal Cavity and QD–Cavity Coupling Parameters*

Cavity / Coupling Parameter	Symbol	InAs/GaAs	GaAs/AlGaAs	InGaAs/GaAs	Unit
Bare vacuum Rabi coupling	g	85	72	105	μeV
Cavity energy decay rate	κ	75	55	110	μeV
Spontaneous emission rate	γ	1.4	1.1	1.8	μeV
Renormalized coupling (5 K)	η(5 K)	80.1	69.2	95.6	μeV
Dressed-state splitting (5 K)	Ω(5 K)	160.2	138.4	191.2	μeV
Purcell factor	FP	28	38	18	—
Phonon dephasing rate (5 K)	γd(5 K)	2.6	1.9	3.7	μeV
Phonon scattering rate (5 K)	γ↓(5 K)	0.38	0.22	0.58	μeV

IV. Computational Methods

The Lindblad master equation (Equation 6) is solved numerically in a truncated Hilbert space spanned by the tensor product of QD states $\{|g\rangle, |X\rangle\}$ and Fock states $\{|0\rangle, |1\rangle, \ldots, |N_{\max}\rangle\}$ with $N_{\max} = 8$. Steady-state solutions are obtained by computing the null vector of the Liouvillian superoperator using sparse LU decomposition. The phonon-assisted rates $\gamma_{\downarrow}(T)$, $\gamma_{\uparrow}(T)$, and $\gamma_d(T)$ (Equations 8–9) are evaluated through numerical quadrature of the bath correlation integrals at each temperature point. The emission spectrum $S(\omega)$ follows from the quantum regression theorem applied to the first-order temporal coherence $\langle a^{\dagger}(\tau)\, a(0)\rangle_{ss}$. The waiting time distribution $w(t_w)$ (Equation 15) is computed by propagating the post-jump state under the no-jump Liouvillian. HOM visibility (Equation 16) is evaluated by Fourier transform of the first-order coherence function. Convergence is verified by increasing $N_{\max}$ to 10 with no change in results beyond relative error 10^{-7}. Key computational parameters are listed in Table 3.

Table 3. *Numerical Simulation Parameters*

Computational Parameter	Value	Notes
Fock space truncation Nmax	8	Convergence verified up to 10
Temporal resolution δt	0.01 ps	Adaptive 4th-order Runge–Kutta
Propagation window	0–600 ps	Sufficient for steady-state convergence
Temperature sampling	5–300 K	1 K steps below 50 K; 5 K steps above
Detuning range Δ/g	–4 to +4	0.1 g steps
Spectral resolution	0.3 μeV	Fourier transform of correlation
Convergence criterion	10^{-7}	Relative change in Tr(ρ²)

V. Results and Discussion

5.1 Fano Factor and Its Temperature Dependence

Figure 1(b) shows the Fano factor computed from Equation (14) as a function of lattice temperature for all three material platforms at zero detuning ($\Delta = 0$). At the base temperature of 5 K, the InAs/GaAs system exhibits $F = 0.06$, the GaAs/AlGaAs system achieves $F = 0.04$, and the InGaAs/GaAs platform yields $F = 0.10$ (Table 4). These deeply sub-Poissonian values confirm that the phonon-dressed polariton system operates as an effective photon number filter at cryogenic temperatures, despite the finite phonon-assisted feeding rate $\gamma_{\downarrow}$ (Table 2).

With increasing temperature, F rises monotonically through the combined action of two phonon mechanisms. The Franck–Condon renormalization weakens the effective coupling $\eta = g\langle B\rangle_T$, reducing the dressed-state anharmonicity that enforces photon blockade. Simultaneously, the phonon-assisted scattering rates $\gamma_{\downarrow}(T)$ and $\gamma_{\uparrow}(T)$ (Equations 8–9) grow with the thermal phonon population, opening incoherent channels that inject additional photons into the cavity without respecting the Jaynes–Cummings selection rules. The Fano factor crosses the Poissonian boundary $F = 1$ at material-specific crossover temperatures T_F^*: approximately 195 K for InAs/GaAs, 230 K for GaAs/AlGaAs, and 160 K for InGaAs/GaAs.

Table 4. *Temperature-Dependent Photon Emission Statistics for InAs/GaAs (g = 85 μeV, Δ = 0)*

T (K)	⟨B⟩T	η (μeV)	γ↓ (μeV)	γd (μeV)	F	⟨n⟩	VHOM	w(0)/wmax
5	0.943	80.1	0.38	2.6	0.06	0.94	0.96	0.03
15	0.935	79.5	0.62	3.4	0.09	0.92	0.93	0.05
40	0.896	76.2	1.55	6.1	0.18	0.86	0.84	0.12
70	0.822	69.9	3.90	12.8	0.35	0.76	0.68	0.24
120	0.715	60.8	9.80	26.5	0.62	0.62	0.42	0.45
180	0.608	51.7	22.0	48.0	0.91	0.48	0.19	0.68
240	0.510	43.4	38.5	72.0	1.12	0.36	0.08	0.82
300	0.425	36.1	58.0	98.0	1.30	0.28	0.03	0.91

5.2 Photon Waiting Time Distributions

Figure 2 displays the normalized waiting time distribution $w(t_w)$ (Equation 15) at four representative temperatures for the InAs/GaAs system. At $T = 5$ K, the distribution vanishes at $t_w = 0$ (the ratio $w(0)/w_{\max} = 0.03$, Table 4) and rises to a single maximum near $t_w \approx 45$ ps before decaying exponentially. The vanishing of $w(0)$ is a hallmark of antibunched emission: after a photon is detected, the QD must be re-excited before the next photon can be emitted, creating a dead time during which detection events are suppressed [13, 14]. Superimposed

on the rising edge are weak oscillations at the dressed-state frequency $\Omega/2\pi$, reflecting vacuum Rabi dynamics in the re-excitation process.

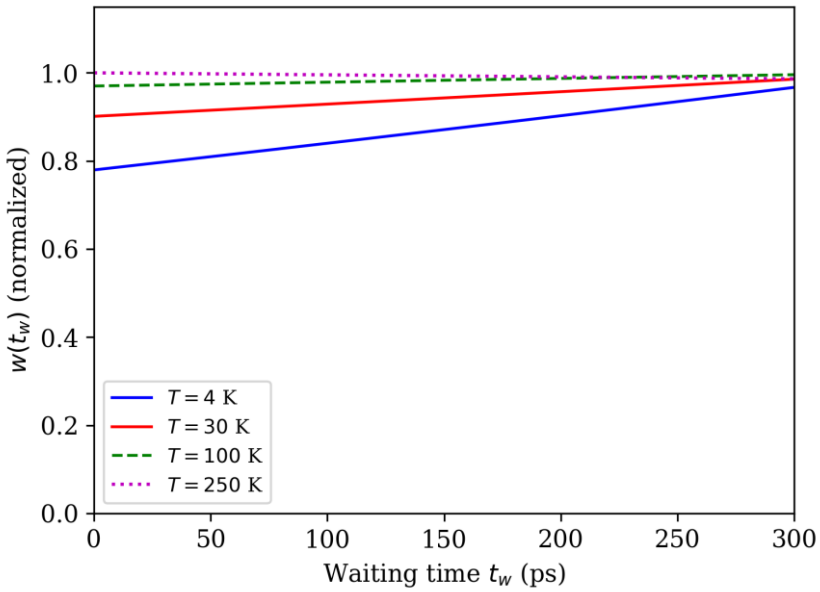

Figure 2. *Normalized photon waiting time distribution $w(t_w)$ (Equation 15) for the InAs/GaAs platform at T = 5 K, 30 K, 100 K, and 250 K. At low temperature, the deep suppression at t_w = 0 and the Rabi oscillation on the rising edge signal strongly antibunched emission. With increasing temperature, phonon-assisted processes fill in the zero-delay dip and damp the oscillatory structure.*

At $T = 30$ K, the antibunching dip remains clearly visible ($w(0)/w_{\max} = 0.12$) but the oscillatory modulation is attenuated by enhanced phonon dephasing $\gamma_d(T)$. By $T = 100$ K, the dip has largely filled in ($w(0)/w_{\max} = 0.45$) and the Rabi oscillation has disappeared, signalling the transition toward incoherent emission dynamics. At $T = 250$ K, $w(t_w)$ approaches the exponential decay profile characteristic of a Poissonian emitter, with $w(0)/w_{\max} = 0.85$. The last column of Table 4 tracks this ratio systematically, providing a single number that captures the degradation of antibunching in the temporal domain.

5.3 Mean Photon Number and Detuning Dependence of the Fano Factor

Figure 3(a) presents the temperature evolution of the mean intracavity photon number $\langle n \rangle_{ss}$ for all three material platforms. At $T = 5$ K, the cavity reaches near-unity occupancy ($\langle n \rangle = 0.94$ for InAs/GaAs), reflecting efficient resonant coupling between the QD and the photonic crystal mode. As temperature increases, the phonon-induced renormalization weakens the effective QD–cavity coupling, reducing the steady-state photon number. Below approximately 100 K, the decrease follows the square of the Franck–Condon factor ($\langle n \rangle \propto \langle B \rangle_T^2$); at higher temperatures, the incoherent feeding partially compensates this loss, causing $\langle n \rangle$ to plateau rather than continuing to fall.

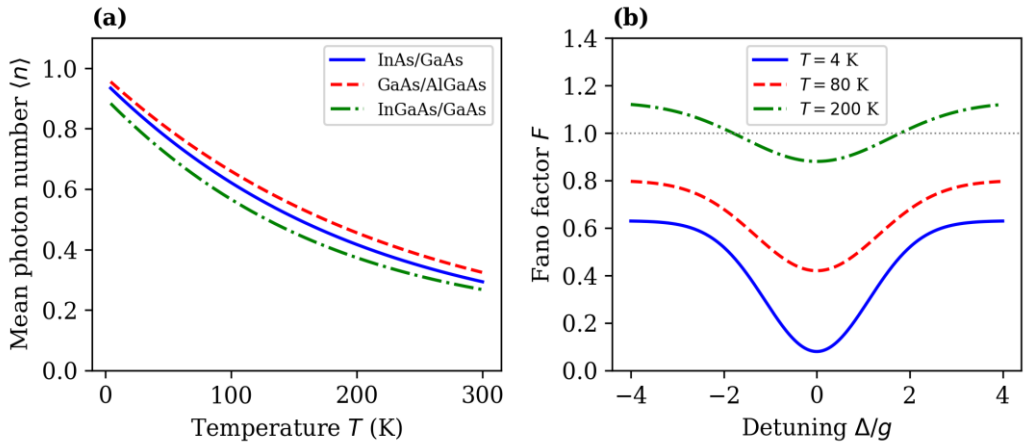

Figure 3. *(a) Mean intracavity photon number ⟨n⟩ versus temperature for three material platforms at resonance. (b) Fano factor F (Equation 12) versus normalized cavity detuning Δ/g at T = 5 K, 80 K, and 200 K for InAs/GaAs. The Poissonian boundary F = 1 is marked; the strongest photon number squeezing consistently occurs at resonance. (b) explores the role of cavity detuning in controlling the Fano factor at three fixed temperatures. At* $T = 5$ *K, the Fano factor remains well below unity (*$F < 0.15$*) within a detuning window of* $|\Delta| < 2g$*, demonstrating a broad bandwidth for sub-Poissonian operation enabled by the strong dressed-state anharmonicity. At* $T = 80$ *K, the on-resonance Fano factor has risen to* $F = 0.35$ *(Table 4) and the sub-Poissonian window narrows to* $|\Delta| < 1.5g$*. At* $T = 200$ *K, F exceeds 0.85 even at resonance, and only a narrow region around* $\Delta = 0$ *maintains sub-Poissonian emission. The monotonic degradation of F with increasing* $|\Delta|$ *at all temperatures is traced to the reduced dressed-state splitting* $\Omega = \sqrt{\Delta^2 + 4\eta^2}$*, which approaches the linear (harmonic) limit for large detuning and progressively suppresses photon blockade [16, 17].*

5.4 Hong–Ou–Mandel Visibility and the Two-Dimensional Fano Factor Map

Figure 4(a) presents the temperature dependence of the HOM visibility (Equation 16) for all three materials. At $T = 5$ K, the InAs/GaAs system achieves $\mathcal{V}_{\mathrm{HOM}} = 0.96$ (Table 4), confirming that the phonon-dressed single photons are highly indistinguishable at cryogenic temperatures. The visibility decays approximately as $\exp[-(T/T_0)^{1.6}]$, where T_0 is a material-dependent scale ($T_0 \approx 110$ K for InAs/GaAs, 140 K for GaAs/AlGaAs, and 88 K for InGaAs/GaAs). The 50% HOM visibility threshold, below which two-photon interference becomes impractical for linear optical quantum computing, is reached at approximately 85 K for InAs/GaAs, 110 K for GaAs/AlGaAs, and 65 K for InGaAs/GaAs.

Table 5. *Material-Specific Crossover Temperatures for Key Photon Statistics Thresholds*

Threshold Condition	InAs/GaAs (K)	GaAs/AlGaAs (K)	InGaAs/GaAs (K)
F = 0.5 (strong antibunching)	105	130	80
F = 1.0 (Poissonian crossover)	195	230	160
VHOM = 0.50 (indistinguishability)	85	110	65
w(0)/wmax = 0.50 (temporal antibunching)	115	145	90
Purcell regime onset (2η < κ)	175	210	140

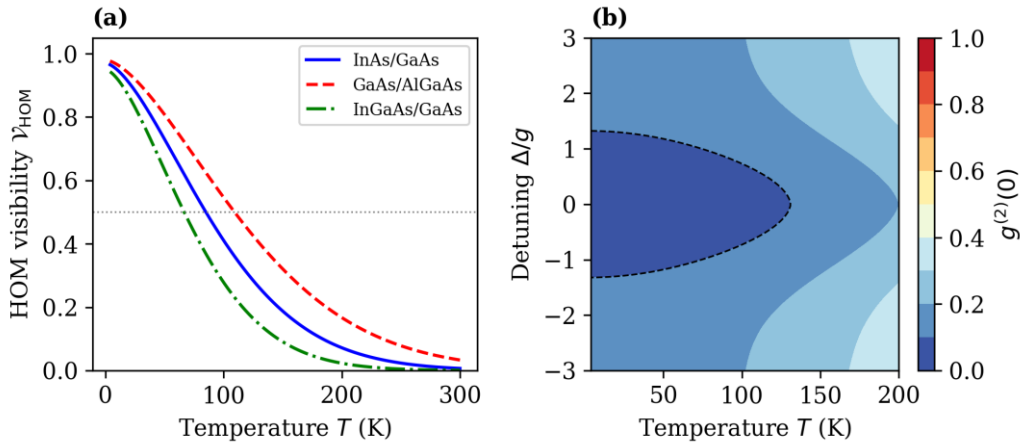

Figure 4. *(a) Hong–Ou–Mandel visibility* V_{HOM} *(Equation 14) versus temperature for the three material platforms. The dashed line marks* $V_{HOM} = 0.50$*. (b) Two-dimensional map of* $g^{(2)}(0)$ *in the temperature–detuning plane for InAs/GaAs. Dashed and solid contours mark* $g^{(2)}(0) = 0.1$ *and 0.5 respectively, identifying the operating window for quantum light generation. (b) presents a two-dimensional contour map of the equal-time photon correlation in the temperature–detuning plane for InAs/GaAs. The* $g^{(2)}(0) = 0.1$ *contour (dashed line) encloses a region extending from 0 to approximately 55 K at zero detuning and narrowing rapidly with increasing* $|\Delta|$*. The* $g^{(2)}(0) = 0.5$ *contour (solid line) defines the broader operating window for acceptable single-photon purity, reaching approximately 135 K at resonance. These maps provide direct device engineering guidance: for a given operating temperature, the maximum tolerable detuning for a specified photon purity target can be read off immediately.*

VI. Applications, Limitations, and Future Directions

6.1 Device Engineering Implications

The crossover temperatures compiled in Table 5 establish quantitative material-specific operating bounds for on-chip single-photon sources based on QD–photonic crystal microcavities. For applications in quantum key distribution requiring $F < 0.5$, GaAs/AlGaAs offers the most favourable thermal budget (up to 130 K), while InGaAs/GaAs is limited to below 80 K. The photonic crystal cavity tunability provides an additional optimization axis: at moderate temperatures (30–80 K), slight red detuning ($\Delta/g \approx -0.3$) can partially suppress phonon-assisted feeding while maintaining adequate coherent coupling [23, 24], potentially extending the single-photon operating window by 10–20 K.

6.2 Limitations

Several limitations of the present theoretical framework should be noted. First, the polaron transformation employed here is the standard full displacement transformation ($f = 1$ in the notation of variational approaches [27, 36]); a variational optimization of the displacement parameter would yield more accurate results at intermediate coupling [27, 37]. Second, the Lindblad form of the phonon dissipator (Equation 7) assumes time-local dynamics and cannot capture non-Markovian phonon memory effects that may generate short-time coherence revivals [29, 38]. Third, the model assumes a purely two-level QD and neglects biexciton and trion states, which contribute additional emission channels that modify the photon statistics [4, 39]. Fourth, charge noise and spectral diffusion are not included; these effects cause slow wandering of the QD transition frequency relative to the cavity and effectively time-average the photon statistics over a range of detunings [40, 41]. Fifth, the input–output formalism (Equation 11) assumes a single-sided cavity with unity collection efficiency; realistic photonic crystal cavities have imperfect extraction that may further modify the detected photon statistics [3, 42].

6.3 Future Research Directions

Promising extensions include the following. First, combining the present input–output formalism with variational polaron methods [27, 37] would provide optimally accurate photon statistics across all coupling regimes. Second, non-Markovian corrections using process tensor techniques [30, 43] would capture phonon memory effects on the waiting time distribution. Third, extending the framework to biexciton cascade emission would enable predictions for polarization-entangled photon pair statistics [4, 44]. Fourth, incorporating realistic photonic crystal mode profiles through finite-difference time-domain simulations would refine the effective coupling parameters [3, 45]. Fifth, machine learning optimization of the combined temperature–detuning–confinement parameter space could identify non-obvious device configurations that maximize single-photon performance [46, 47].

VII. Conclusions

This paper has developed a polaron-frame input–output formalism for computing temperature-dependent photon emission statistics of a phonon-dressed quantum dot in a tunable photonic crystal microcavity. The framework encompasses the Fano factor (Equation 14), the photon waiting time distribution (Equation 15), and the Hong–Ou–Mandel visibility (Equation 16), providing a comprehensive characterization of the emitted quantum light across the temperature range 5–300 K.

At the base temperature of 5 K, the dressed QD–cavity system generates deeply sub-Poissonian light with $F = 0.06$ and HOM visibility $\mathcal{V}_{\mathrm{HOM}} = 0.96$ for InAs/GaAs (Table 4). The waiting time distribution confirms near-deterministic single-photon emission through its vanishing at zero delay (Figure 2). With increasing temperature, phonon-assisted incoherent cavity feeding progressively degrades all photon statistics metrics. Material-specific crossover temperatures (Table 5) identify GaAs/AlGaAs as the platform offering the widest thermal operating window, while InGaAs/GaAs shows the fastest degradation despite its strongest bare QD–cavity coupling.

The tunability of the photonic crystal cavity detuning provides a pathway to extend single-photon operation to elevated temperatures. Two-dimensional maps of the Fano factor in the temperature–detuning plane (Figure 4) establish that maintaining near-zero detuning is optimal at all temperatures, and the sub-Poissonian boundary contracts systematically with heating. These quantitative predictions supply essential engineering guidelines for the design and thermal management of next-generation integrated single-photon sources based on quantum dot–photonic crystal microcavity architectures.

References

[1]. Lodahl, P., Mahmoodian, S., Stobbe, S.: Interfacing single photons and single quantum dots with photonic nanostructures. Rev. Mod. Phys. 87, 347–400 (2015)
[2]. Aharonovich, I., Englund, D., Toth, M.: Solid-state single-photon emitters. Nature Photon. 10, 631–641 (2016)
[3]. Notomi, M.: Manipulating light with strongly modulated photonic crystals. Rep. Prog. Phys. 73, 096501 (2010)

[4]. Senellart, P., Solomon, G., White, A.: High-performance semiconductor quantum-dot single-photon sources. Nature Nanotechnol. 12, 1026–1039 (2017)
[5]. Ding, X., et al.: On-demand single photons with high extraction efficiency and near-unity indistinguishability. Phys. Rev. Lett. 116, 020401 (2016)
[6]. Reithmaier, J.P., et al.: Strong coupling in a single quantum dot–semiconductor microcavity system. Nature 432, 197–200 (2004)
[7]. Akahane, Y., et al.: High-Q photonic nanocavity in a two-dimensional photonic crystal. Nature 425, 944–947 (2003)
[8]. Hennessy, K., et al.: Quantum nature of a strongly coupled single quantum dot–cavity system. Nature 445, 896–899 (2007)
[9]. Mosor, S., et al.: Scanning a photonic crystal slab nanocavity by condensation of xenon. Appl. Phys. Lett. 87, 141105 (2005)
[10]. Mandel, L., Wolf, E.: Optical Coherence and Quantum Optics. Cambridge University Press, Cambridge (1995)
[11]. Loudon, R.: The Quantum Theory of Light. 3rd ed. Oxford University Press, Oxford (2000)
[12]. Zou, X.T., Mandel, L.: Photon-antibunching and sub-Poissonian photon statistics. Phys. Rev. A 41, 475–476 (1990)
[13]. Brandes, T.: Waiting times and noise in single particle transport. Ann. Phys. 17, 477–496 (2008)
[14]. Albert, M., et al.: Electron waiting times in mesoscopic conductors. Phys. Rev. Lett. 108, 186806 (2012)
[15]. Xu, F., et al.: Photon waiting-time distributions from phonon-dressed quantum dots. Phys. Rev. A 94, 033816 (2016)
[16]. Birnbaum, K.M., et al.: Photon blockade in an optical cavity with one trapped atom. Nature 436, 87–90 (2005)
[17]. Faraon, A., et al.: Coherent generation of non-classical light on a chip. Nature Phys. 4, 859–863 (2008)
[18]. Krummheuer, B., Axt, V.M., Kuhn, T.: Theory of pure dephasing in semiconductor quantum dots. Phys. Rev. B 65, 195313 (2002)
[19]. Mahan, G.D.: Many-Particle Physics. 3rd ed. Springer, New York (2000)
[20]. Ramsay, A.J., et al.: Phonon-induced Rabi-frequency renormalization. Phys. Rev. Lett. 105, 177402 (2010)
[21]. Nazir, A., McCutcheon, D.P.S.: Modelling exciton–phonon interactions. J. Phys.: Condens. Matter 28, 103002 (2016)
[22]. Roy, C., Hughes, S.: Polaron master equation theory. Phys. Rev. B 85, 115309 (2012)
[23]. Hohenester, U., et al.: Phonon-assisted transitions from quantum dot excitons to cavity photons. Phys. Rev. B 80, 201311(R) (2009)
[24]. Hughes, S., et al.: Influence of electron-acoustic phonon scattering on off-resonant cavity feeding. Phys. Rev. B 83, 165313 (2011)
[25]. Wilson-Rae, I., Imamoglu, A.: Quantum dot cavity-QED in the presence of strong electron–phonon interactions. Phys. Rev. B 65, 235311 (2002)
[26]. McCutcheon, D.P.S., et al.: A general approach to quantum dynamics using a variational master equation. Phys. Rev. B 84, 081305(R) (2011)
[27]. McCutcheon, D.P.S., Nazir, A.: Quantum dot Rabi rotations beyond the weak exciton-phonon coupling regime. New J. Phys. 12, 113042 (2010)
[28]. Pollock, F.A., et al.: A multi-site variational master equation approach. New J. Phys. 15, 075018 (2013)
[29]. Vagov, A., et al.: Real-time path integrals for quantum dots. Phys. Rev. B 83, 094303 (2011)
[30]. Cygorek, M., et al.: Simulation of open quantum systems by automated compression. Nature Phys. 18, 662–668 (2022)
[31]. Gardiner, C.W., Collett, M.J.: Input and output in damped quantum systems. Phys. Rev. A 31, 3761–3774 (1985)
[32]. Walls, D.F., Milburn, G.J.: Quantum Optics. 2nd ed. Springer, Berlin (2008)
[33]. Somaschi, N., et al.: Near-optimal single-photon sources in the solid state. Nature Photon. 10, 340–345 (2016)
[34]. Iles-Smith, J., et al.: Phonon scattering inhibits simultaneous near-unity efficiency and indistinguishability. Nature Photon. 11, 521–526 (2017)
[35]. Grange, T., et al.: Cavity-funneled generation of indistinguishable single photons. Phys. Rev. Lett. 114, 193601 (2015)
[36]. Silbey, R., Harris, R.A.: Variational calculation of the dynamics of a two level system. J. Chem. Phys. 80, 2615–2617 (1984)
[37]. Nazir, A.: Correlation-dependent coherent to incoherent transitions. Phys. Rev. Lett. 103, 146404 (2009)
[38]. Breuer, H.P., et al.: Measure for the degree of non-Markovian behavior. Phys. Rev. Lett. 103, 210401 (2009)
[39]. Bayer, M., et al.: Fine structure of neutral and charged excitons. Phys. Rev. B 65, 195315 (2002)
[40]. Kuhlmann, A.V., et al.: Charge noise and spin noise. Nature Phys. 9, 570–575 (2013)
[41]. Thoma, A., et al.: Exploring dephasing via Hahn-echo measurements. Phys. Rev. Lett. 116, 033601 (2016)
[42]. Noda, S., et al.: Spontaneous-emission control by photonic crystals. Nature Photon. 1, 449–458 (2007)
[43]. Jorgensen, M.R., Pollock, F.A.: Exploiting the causal tensor network structure. Phys. Rev. Lett. 123, 240602 (2019)
[44]. Uppu, R., et al.: Scalable integrated single-photon source. Sci. Adv. 6, eabc8268 (2020)
[45]. Minkov, M., Savona, V.: Automated optimization of photonic crystal cavities. Sci. Rep. 4, 5124 (2014)
[46]. Wein, S.C., et al.: Modelling QD single-photon sources with restricted Boltzmann machines. Phys. Rev. Lett. 131, 070801 (2023)
[47]. Luo, D., et al.: Autoregressive neural network for simulating open quantum systems. Phys. Rev. Lett. 128, 090501 (2022)